The Influence of Gas Extraction on Bubble Dynamics

by

Corey D. Juarez

A PROJECT

submitted to

Oregon State University

University Honors College

in partial fulfillment of
the requirements for the
degree of

Honors Baccalaureate of Science in Mechanical Engineering (Honors Associate)

Presented March 9, 2015

Commencement June 2015

ABSTRACT OF THE THESIS OF

Corey D. Juarez for the degree of Honors Baccalaureate of Science in Mechanical Engineering presented on March 9, 2015. Title: The Influence of Gas Extraction on Bub-Dynamics.

Abstract approved:

Deborah V. Pence

A new thermal management method for hotspots on microprocessors is under development that employs confined pool boiling with vapor extraction at pre-determined nucleation sites. Extraction is accomplished by locating a vacuum chamber constructed out of a glass tube and a hydrophobic membrane directly above a nucleation site. In order to elucidate the underlying physics of vapor extraction, an adiabatic experiment was conducted to isolate the hydrodynamics. Air was injected at a rate of 90 mm^3/s through an orifice of diameter 0.5 mm submerged in water at ambient temperature to generate isolated gas bubbles. The effect of varying the gap height between the orifice and the extraction surface was studied over a range from 1.22 mm to 3.49 mm. Bubble departure diameters were observed to be 80% of the gap height, and bubble departure frequencies were observed to be inversely related to departure diameter. Correlations for departure diameter, rupture diameter, and departure frequency were developed. The foundations of a theoretical static force balance to determine confined departure diameters was developed along with a theoretically based transient bubble diameter model to predict bubble departure frequency. A detailed design of the adiabatic test device is also included.

Key Words: submerged orifice, confined pool boiling, gas extraction

Corresponding e-mail address: coreyjuarez@gmail.com

Honors Baccalaureate of Science in Mechanical Engineering project of Corey D. Juarez presented on March 9, 2015.

APRROVED:

Deborah V. Pence, Mentor, representing Mechanical Engineering

---

James Liburdy, representing Mechanical Engineering

Randall Fox, representing Mechanical Engineering

Toni Doolen, Dean, University Honors College

I understand that my project will become part of the permanent collection of Oregon State University, University Honors College. My signature below authorizes release of my project to any reader upon request.

Corey D. Juarez

Acknowledgements

With respect to this project specifically, I would like to thank Dr. Pence for her patience, guidance, and encouragement. She committed many hours in her mentorship over the last year and a half. I would also like to express my gratitude to Randall Fox, who has graciously helped me out it times of need. I could have not completed my thesis project without his generosity. I would also like to thank Dr. Liburdy, for his guidance while I was trying to decide what to do for my thesis project, and for his witty sense of humor. One of my favorite parts of this experience was meeting with Dr. Pence, Randall, and Dr. Liburdy on a weekly basis to discuss our research.

I would also like to thank Cameron Planck for helping me out with analysis while I was trying to meet a deadline, and for the healthy distractions throughout our time in pro-school. Most importantly, I would also like to thank my husband Cory Gerlach for being a great listener, supporting me in all of my endeavors, and for his patience. I would not be where I am today without him.

I would also like to add that this project would not have been possible without the financial support of the University Honors College, the Oregon State Research Office (URISC), and the Oregon NASA Space Grant Consortium.

Contents

List of Figures

List of Tables

Nomenclature

Symbols

$\dot{m}$	Mass flow rate	kg/m^2
A	Area	m^2
D	Diameter of 3-D objects: bubbles	m
d	Diameter of 2-D objects: contact areas	m
F	Force	N
f	Frequency	$1/s^{-1}$
g	Gravity	m/s^2
H	Extraction surface gap height	m
I	Image	$-$
P	Pressure	N/m^2
St	Strouhal number	$-$
t	Time	$seconds$
V	Volume	m^3
v	Velocity	m/s

Greek Symbols

δ	Membrane thickness	m
κ	Permeability	m^2
μ	Dynamic viscosity	$kg/m-s$
ϕ	Angle of solid wedge	$degrees$
ρ	Density	kg/m^3
σ	liquid-vapor surface tension	N/m
θ	Instantaneous contact angle	$degrees$
θ_0	Young's contact angle	$degrees$

Subscripts

B	Net buoyancy

bg	Background
bub	Bubble
D	Departure
e	Exit
eff	Effective
ext	Extraction
G	Growth
g	Gas
I	Regime I
II	Regime II
III	Regime III
l	Liquid
o	Orifice
$orig$	Original
R	Rupture
$slice$	slice of image one pixel in height
sup	Supply
UD	Unconfined departure
w	Wetting

Bubble Events

C	Contact
D	Departure
E	Extraction
I	Inception
R	Rupture

1 Introduction and Background

A new method for the thermal management of microprocessors that employs localized in-situ vapor extraction is being developed to meet the spatio-temporal cooling demands of microprocessors. The need for new techniques is driven by the fact that that over time, microprocessors have not only become smaller, but they have also seen drastic increases in performance. As a result of increased performance and reductions in size, the power density of microprocessors have increased, resulting in thermal hotspots [2, 3, 4]. The thermal management of hotspots is important because a microprocessor's performance and mean time to failure are both temperature dependent [4, 3].

A promising approach for the thermal management of microprocessors is to use two-phase flow in microchannels. This method is attractive because of the latent heat associated with phase change [3]. Employing phase change in microchannels presents unique challenges though, as researchers have shown that flow instabilities and high pressure drops are introduced that can actually have an adverse effect on the effectiveness of such devices by causing dry out which can lead to critical heat flux conditions [5, 6]. This led Apreotesi et al. [5] to study the effects of applying vapor removal to microscale fractal-like branching microchannel flow networks. Similar work was conducted by David et al. [7, 8] by applying vapor extraction to several different microchannel configurations. In addition, the latter group conducted a computational fluid dynamics analysis [9]. The results of studies that address vapor removal from microchannel heat sinks show that lower operating temperatures can be maintained with lower channel pressure drops.

Vapor extraction is a technique that confines bubble growth to some known distance, or gap height, by locating a vacuum chamber with a porous hydrophobic membrane

attached to the end of it above a nucleation site. The bubble nucleates, grows, and then ruptures after making contact with the membrane. Following the bubble's rupture, vapor is extracted from the bubble as a result of a pressure differential across the membrane. This added effect causes bubble departure from the supply surface at a diameter less than that of a departing bubble that is unconfined. By varying the gap height, the bubble departure diameter and frequency can be controlled, which is expected to have an effect on the effective area of heat transfer and the time averaged heat transfer coefficient [1].

Although ultimately intended for thermal management, the inherent complexity of physical phenomena during boiling has motivated an adiabatic study with the goal of elucidating the underlying hydrodynamics of a bubble experiencing extraction. While using air injected through an orifice to study bubble dynamics is nothing new for unconfined conditions, using it to study confined extraction is. A recent study by Fazeli et al. [10] used air injected through orifices to visualize bubble dynamics during venting, where venting occurs by pressurizing the liquid chamber and venting air through a membrane to the ambient.

There are two main consideration to be taken into account in designing an adiabatic experiment using a submerged orifice; the behavior of the three phase contact line at the edge of the orifice, and whether or not constant volumetric flow rate through, or constant pressure conditions across the orifice are desired. The work of Gerlach et al. [11] studied the effect of Young's contact angle on the behavior of the three phase contact line at the orifice. They show that based on Gibb's inequalities [12] there are two possible modes of bubble growth from an orifice: Mode A refers to bubble growth where the three phase contact line remains attached at the orifice rim, and Mode B refers to bubble growth where the three phase contact line does not remain attached

to the orifice rim during bubble growth, which is referred to as spreading.

Constant flow conditions refer to bubbles forming without a"wait time" between subsequent bubbles and the volumetric growth rate of the bubble remains essentially constant throughout its life cycle. A study by Terasaka et al. [13] showed that this can be accomplished by maintaining a pressure drop across the orifice that is large enough to overcome the capillary forces at the orifice. Satyanarayan et al. [14] define constant pressure conditions as maintaining a constant pressure in the chamber below the orifice, which results in a nonlinear volumetric growth rate of a bubble.

Covered in detail in this thesis are the design of the adiabatic test device and the preliminary observations that are used to develop the foundation of a theoretically-based static force balance to predict bubble departure diameter and a theoretically based time-dependent bubble diameter model to predict bubble departure frequency. See also Fox et al. [1]

2 Experimental Test Facility

The experimental test facility in Fig. 1 consists of a test chamber where bubbles are created and extracted, halogen back lighting, a U-tube manometer to measure the pressure drop across the orifice, a syringe pump to inject air through the orifice, and a Nikon J5, which was used to record video footage of the extraction process at a frame rate of $1200 fps$. The extraction chamber in Fig. 2 consists of a glass tube connected by plastic tubing to a vacuum source. The vacuum was created and varied by suspending weights from a set of 10 ml syringes. The pressure inside of the extraction chamber was measured with a previously calibrated differential pressure transducer (OMEGADYNE PX 409-015DWUV) recorded at 1000 Hz. The pressure

in the extraction chamber was maintained at 15 kPa for this study. Photographs of the experimental set-up can be viewed in Appendix A.

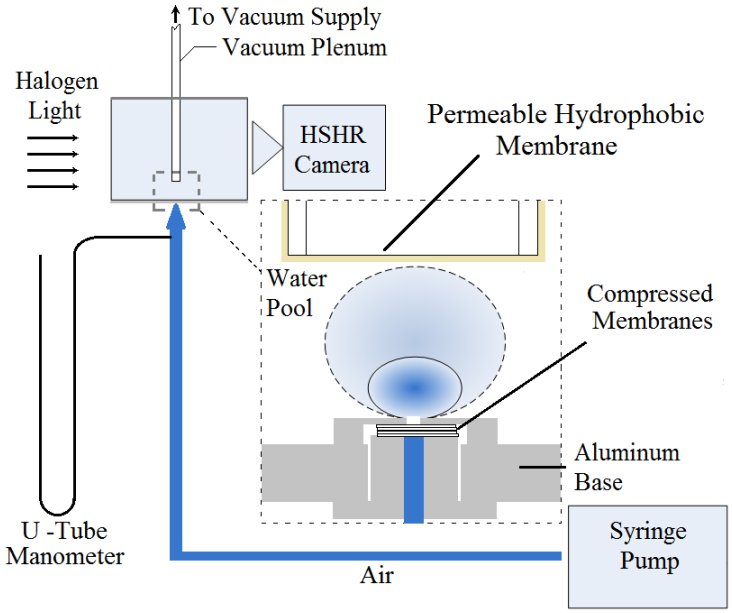

Figure 1: Adiabatic test facility

2.1 Extraction Chamber

A hydrophobic PTFE membrane with laminated support material from Sterlitech with a specified pore diameter of 0.45 μm, a porosity of 55%, and a thickness of 15.6 μm was used for the extraction surface in Fig. 3 that confines the bubbles growth. The extraction surface was then secured to the bottom of a glass tube (4.2 mm OD, 2.1 mm ID) using high temperature RTV silicone. High temperature RTV was used because the extraction chamber is identical to the one used in the diabatic experiments by Fox et al. [1]. The extraction surface can be adjusted vertically to adjust the gap height, H, above the orifice plate.

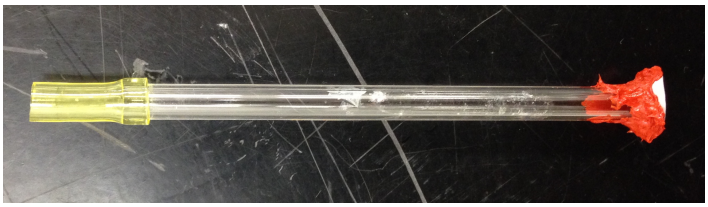

Figure 2: Side view of the extraction chamber

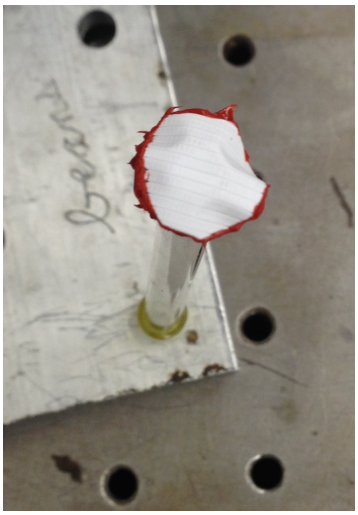

Figure 3: The extraction membrane attached to the end of the glass tube that makes up the extraction chamber

2.2 Test Chamber Design

The design requirements and the design of the test chamber are detailed in this section.

2.2.1 Design Requirements and Considerations

Unlike in boiling where the diameter of the three phase contact line at the heated surface changes, a submerged orifice experiment can be designed in such a way that the gas bubble's three phase contact line remains attached at the rim of the orifice throughout the life cycle of the bubble. By ensuring that the three-phase contact line remains attached to the orifice rim, the diameter of the bubble's attachment is known. This diameter is used to assess the surface tension force at the base of the bubble.

Accurately assessing this force during boiling has proven to be one of the most challenging aspects of developing pool boiling force balance models [15]. Furthermore, the orifice can also be designed in such a way that the flow-rate is considered to be "constant". That is, the bubbles volumetric growth rate is linear and bubbles form instantaneously following the departure of a preceding bubble.

The design requirements for the test chamber are as follows:

- A constant flow-rate should be achieved through the orifice in order to ensure there is no "wait time" between the departure of one bubble and the inception of another.
- The three phase contact line should remain pinned to the rim of the orifice during the bubbles life cycle in order to more accurately assess the surface tension force on the bubble at the orifice.

2.2.2 Orifice Plate

The orifice plate was constructed out of aluminum with the overall dimensions of 1.25" X 1.25" X 0.25". A pocket was machined out of the bottom of the plate that is 0.5" X 0.5" X 0.21" leaving the center of the orifice plate with a thickness of 0.04" or about 1 mm. A hole of diameter 0.5 mm was drilled through the center of the plate. Air was injected through the orifice at a constant volumetric flow rate using a Cole Parmer programmable syringe pump. A single injection rate of 90 mm^3/s was used in this study. A detailed drawing of the orifice plate can be found in Appendix B.

The design of the orifice plate was based on the work by Gerlach et al. [11], who studied the effects of Young's contact angle on the behavior the three-phase contact line at the rim of a submerged orifice in water. The two modes of contact line behavior during a bubble's life cycle are Mode A where the contact line remains attached to

the rim of the orifice and Mode B where the contact line spreads, and does not stay attached to the orifice rim. Gibb's inequalities state that if the instantaneous contact angle θ meets the following condition

$$\theta_0 \leq \theta \leq (180^\circ - \phi) + \theta_0 \tag{1}$$

where θ_0 is Young's contact angle, and ϕ is the angle of the solid wedge seen in Fig.4, then the three-phase contact line will stay attached to the orifice rim throughout its growth up until departure. However, if $\theta \leq \theta_0$ is ever reached, then Mode B contact line behavior will occur. For the single working fluid chosen for this experiment Young's contact angle is purely a function of the surface energy of the material selected for the orifice plate.

Based on Eq.(1), it becomes apparent that in order to sustain very small instantaneous contact angles during the life cycle, then materials with the smallest Young's contact angle between water and air should be chosen for the orifice plate. Thus high surface energy materials should be chosen if Mode A behavior is desired.

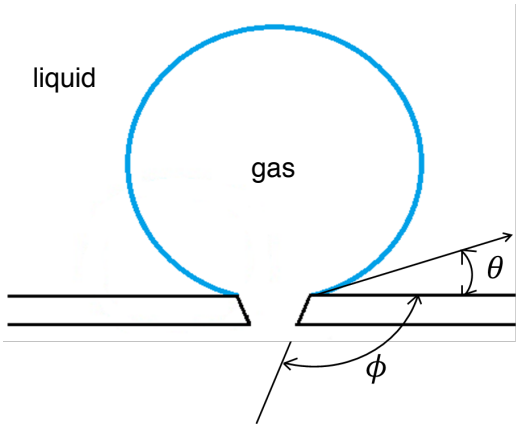

Figure 4: Illustrating the angles used in Gibb's inequalities for three-phase contact line at the edge of a solid

Bernardin et al. [16] performed an experimental study on the advancing contact angle on aluminum. They tabulated previously reported advancing contact lines for water and other metals as part of their study, which serves as an excellent guide for material selection. Aluminum was chosen as the material for this experiment because it has a sufficiently low advancing contact angle, and it is readily available. Based on the study by Gerkach et al. [11], if smaller orifice diameters are to be used, it may be necessary to choose a material with a lower advancing contact angle, such as magnesium or titanium.

The surface treatment and condition of the orifice plate is also an important consideration. The surface energy can be greatly affected by how smooth or rough the surface is. It should be noted that roughening the surface can increase the surface energy of the material, reducing its Young's contact angle. On the other hand polishing the surface can decrease the surface energy of a high surface energy material. Care should be taken when preparing the orifice plate prior to collecting data. Oxidation of the aluminum surface can cause a drop in surface energy, so it may be necessary to roughen the surface with 1500 grit wet sandpaper prior to data collection. If this step is not taken Mode B three-phase contact line behavior may occur at the orifice.

2.2.3 Test Chamber Base

The design of the test chamber in Fig. 5 plays a significant role in the ability to achieve a constant volumetric flow-rate through the orifice. In order to achieve this, the modified constant-flow condition presented by Terasaka and Tsuge [13] was used

$$\Delta P_o > \frac{4\sigma}{d_o} \tag{2}$$

where ΔP_o is the pressure drop across the orifice, σ is the interfacial surface tension between the liquid and vapor phases, and d_o is the diameter of the orifice. This relationship, an apparent application of the Young-Laplace equation, says that as long as the pressure drop is greater than the right hand side then constant flow conditions exist. If a high enough pressure drop is not maintained across the orifice, then after a bubble detaches the capillary forces on the residual bubble that is left could be great enough to actually "suck" it back into the the orifice and cause a "wait time" between subsequent bubbles while the pressure on the feed side of the orifice plate grows large enough to overcome both the capillary forces.

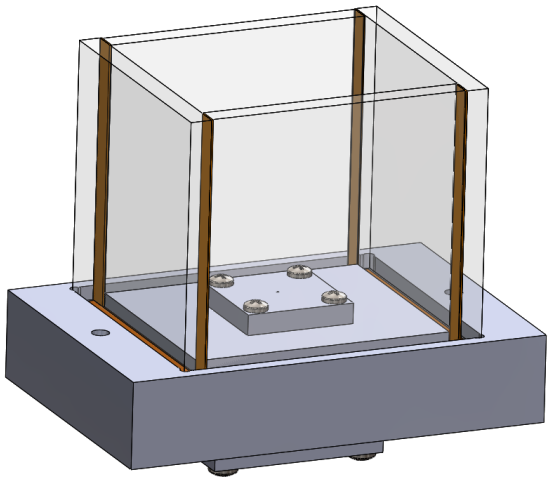

Figure 5: Three dimensional model of test chamber assembly

A common technique for meeting this criteria is the use of packed beads beneath the orifice [13]. Although this method has been proven to be successful, it is a cumbersome technique and difficult to design in such a way that would support a wide range of volumetric flow-rates. A new, more versatile, and compact technique has been developed for this experiment.

The base of the test chamber Fig. 6 was designed in such a way that an adjustable

"stack-up" of porous membranes could be compressed under the orifice plate. The pressure drop can be adjusted by either changing the number and/or porosity of the membranes in the stack-up, or by adjusting the compressive force that is applied to the stack-up by using the membrane compactor.

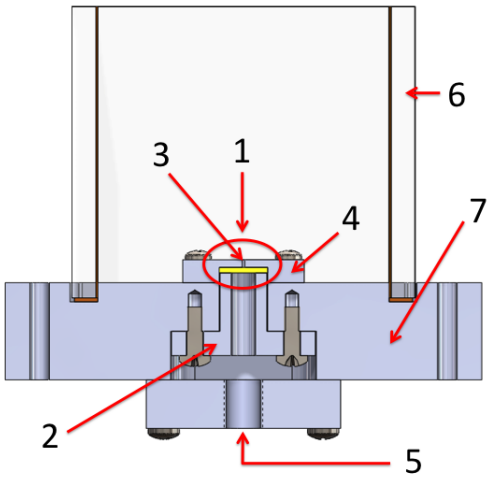

Figure 6: Cross section view of test chamber assembly. 1: membrane stack-up between orifice plate and membrane compactor, 2: membrane compactor, 3: orifice, 4: orifice plate, 5: air-inlet, 6: glass walls, 7: bubble chamber base

2.3 Imaging System

Videos were taken of the bubbles using a Nikon J5 camera with a AF Micro Nikkor 60mm lens (resolution 36.9 $\mu m/pixel$). The Nikon J5 is capable of capturing images at 1200 fps. To determine the resolution, a removable calibration pin (a precision ground stainless steel pin with a diameter of 4 mm) was inserted into the orifice plate in the same plane of the bubble that is perpendicular to the camera. Images were then taken of the pin and Canny edge detection was then performed on the images. The diameter of the pin was then determined in terms of number of pixels. The measured pin diameter was then divided by the total number of pixels resulting in the length represented by each pixel ($length/pixel$).

3 Data Reduction

3.1 Image Processing

An image processing routine that is similar to the one used by Xie [17] was used that employs image subtraction to isolate a bubble from its surroundings, i.e. the extraction chamber. Canny edge detection is then used to determine the bubble's outline, producing a two-dimensional binary image. Figure 7 shows this process applied to a single frame. The background image, Fig. 7b, is subtracted from the original image, Fig. 7a, resulting in the image in Fig. 7c. The results of applying Canny edge detection to Fig. 7c are shown in Fig. 7d. The equation from Xie [17] that is used to perform background subtraction is

$$I = 255 - |I_{bg} - I_{orig}| \tag{3}$$

where I is the resulting image, Fig. 7c, I_{bg} is the background image in Fig. 7b, and I_{orig} is the original image, Fig. 7a.

(a) Original (b) Background (c) Subtracted (d) Canny

Figure 7: Image processing steps

Fox et al. [1] tested the image processing algorithm by taking images of a ball bearing of 7.15 mm diameter, and then calculating its volume. The volume determined by the algorithm was found to be within 1.7% of the actual volume.

3.2 Data Analysis

Once a bubble's outline has been found using Canny edge detection, analysis of the bubble can occur. In order to determine the total volume of a bubble, two dimensional slices of the frame are taken that are one pixel in height and converted into three dimensional discs assuming that they are axisymetrical about the axis normal to the orifice plate. The diameter of the disk is taken to be the distance in pixels between the two outer most pixels of the slice. Knowledge of the pixel dimensions in units of $length/pixel$, allows for calculating the volume of a slice. This process is repeated along the entire vertical axis of the bubble. Summing the volumes of each disk provides a measure of the total volume of the bubble

$$V_{slice} = \pi d_{slice}^2 * (length/pixel) \tag{4}$$

$$\sum_{n=1}^{N} V_{slice_i} = V_{bub,total} \tag{5}$$

where N is the total number of slices that make up the height of the bubble. The effective diameter of the bubble can then be deduced from the volume

$$D_{eff} = \sqrt[3]{\frac{6V_{bub,total}}{\pi}} \tag{6}$$

From this point on the effective diameter of a bubble, D_{eff}, will be referred to simply as the diameter, D, where D now refers to the diameter of a spherical bubble that has a volume equal to the total bubble volume, $V_{bub,total}$.

3.3 Uncertainty

A thorough uncertainty analysis on the data in this thesis was conducted in the study by Fox et al. [1]. While the uncertainty values for statistically averaged data, such as bubble diameters, times, and frequency are included in the results, values included in

the propagation of uncertainty using the Kline-McKlintock are included in Table 1.

Table 1: Uncertainties reported by the manufacturer, calibration uncertainty, and assumed uncertainties used in propagation analyses.

Parameter	**Uncertainty**	**Source**
gap height, H	$\pm 0.02\ mm$	assumed
measured bubble diameter, D	$\pm 0.02\ mm$	calibration
time measurements, t	$\pm 0.42\ ms$	calibration
transducer calibration, ΔP	$\pm 0.2\ kPa$	calibration
syringe pump, $\dot{V}_{sup}$	$\pm 2.3\ mm^3/s$	manufacturer
membrane permeability, k	$\pm 1 \times 10^{-15}\ m^2$	manufacturer
membrane thickness, δ	$\pm 2.5\ \mu m$	manufacturer
extraction area, A_{ext}	$\pm 3\%\ (max)$	assumed

4 Experimental Results

4.1 Bubble Types Observed

Bubbles were generated from the submerged orifice and high speed videos were taken of their growth and extraction. The bubbles were extracted through a confining hydrophobic porous surface at prescribed gap heights, H, above the orifice plate. Observing the effects of varying H on the hydrodynamics is the primary interest of this study. The bubbles observed while reviewing the videos where classified into three main types:

- Type 1: bubbles that grow and rupture before they depart from the orifice
- Type 2: bubbles that grow and coalesce with the preceding bubble before they depart from the orifice

- Type 3: bubbles that depart from the orifice before they rupture at the extraction surface

4.2 Events Observed During a Confined Bubble's Life Cycle

Type 1 bubbles are expected to be the most applicable for spatio-temporal cooling because their behavior is more predictable, and it is thought that their departure diameter and departure frequency can be adjusted by varying the gap height between the orifice plate and the extraction surface. The events observed during a Type 1 bubbles life cycle are:

- (I) Inception - The initiation of the bubble
- (C) Contact - When the bubble makes contact with the extraction surface
- (R) Rupture - When the bubble ruptures at the extraction surface
- (D) Departure - When the bubble departs from the orifice
- (E) Extinction - When the bubble has been fully extracted through the membrane

4.3 Characterizing Type 1 Bubbles

The experimental component of this study focuses on characterizing the departure diameter and frequency of Type 1 bubbles. The time at which each of the Type 1 events occur and the effective diameter at each event is also determined. Each event can be identified by a sequential frame number in a high speed video. To determine the time corresponding to each event occurrence, the difference between the frame number at inception and the frame number at an event is used in combination with the frame rate of the video to calculate a time.

4.3.1 Bubble Diameter as a Function of Time

The diameter of ten consecutive bubbles are plotted as a function of time in Fig. 8 for the test case $H = 1.22\ mm$. For each bubble the experimentally determined diameter at the point of rupture, D_R, and the diameter at departure, are also noted. Figure 8 shows that there is a small degree of scatter with good repeatability where rupture, departure, and extinction occur. However, there are some fluctuations in diameter between rupture and departure. This may be due to a dynamic three-phase contact line on the extraction surface resulting in a time varying extraction area and thus extraction rate. The average rupture and departure diameters are 1.53 mm and 0.97 mm respectively, and the average departure frequency is 33 Hz. These results are tabulated in Table 2 along with other test cases where the maximum uncertainty is $\pm 0.02\ mm$ for diameter and gap height and $\pm 3\ Hz$ for frequency.

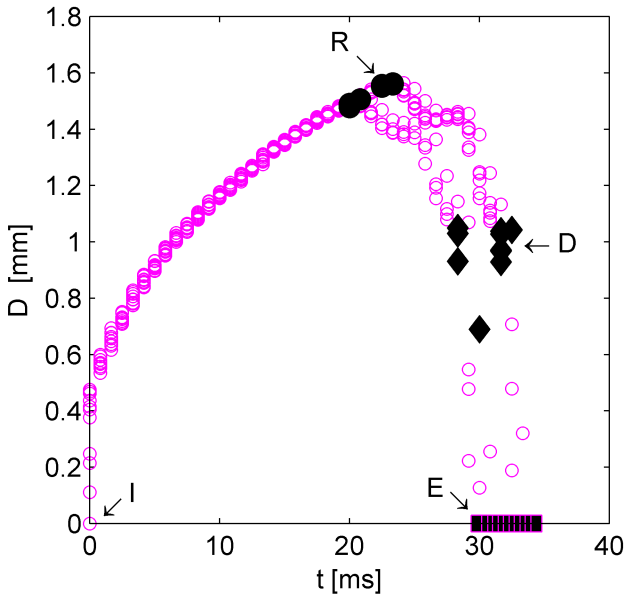

Figure 8: Bubble diameter as a function of time for ten consecutive bubbles at a gap height $H = 1.22\ mm$ where the identified events are I: inception, R: rupture, D: departure, and E: extinction [1]

4.3.2 The Relationship Between Rupture Diameter, Departure Diameter, and Departure Frequency

The data presented in Table 2 for gap heights of 1.22 mm, 2.14 mm, and 3.25 mm is plotted in Fig. 9. Also plotted in figure 9 are data from the diabatic study simultaneously conducted in the laboratory and presented in Fox et al. [1]. It appears as though that with an increase in gap height there are both increases in a bubble's rupture, D_R, and departure, D_D, diameter which are accompanied by a decrease in departure frequency, f_D. More adiabatic data will need to be analyzed in order to confirm this trend, but as was discussed in the study by Fox et al. [1], the trends observed for the adiabatic case are in agreement with what is observed in diabatic confined extraction.

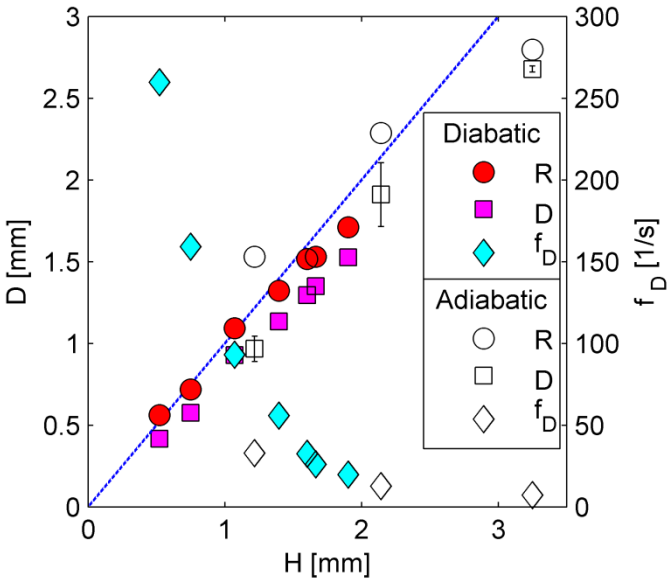

Figure 9: Bubble departure diameter, D_D, bubble rupture diameter, D_R, and bubble departure frequency, f_D, versus gap height, H. [1]

Table 2: Tabulated values for bubble departure diameter and departure frequency for all test cases, including. Included are those determined via experimental observation, correlations, and preliminary models.

		Adiabatic			
	H (mm)	1.22	2.14	3.25	∞
	Number of Bubbles	10	10	10	10
D_R (mm)	Experiments	1.53	2.29	2.80	N/A
	Rupture Correlation: Eq. (7)	1.60	2.17	2.85	N/A
D_D (mm)	Experiments	0.97	1.91	2.68	2.88
	Departure Correlation: Eq. (8)	1.02	1.80	2.73	N/A
	Force Balance	0.97	1.91	2.68	2.85
F_D (Hz)	Experiments	33	13	7	7
	Strouhal Correlation: Eq. (12)	32	14	6	N/A
	Diameter Model	29	15	7	7

4.3.3 Correlations for Rupture Diameter, Departure Diameter, and Departure Frequency

Correlations for bubble rupture and departure diameters were developed as a function of gap height for the range presented in Table 2 and in Fig. 9 by performing linear regression analyses. The correlations are presented here, where rupture diameter, D_R, and departure diameter, D_D, have the units of mm and the associated standard errors of the fit are included in parenthesis.

$$D_R = 0.62H + 0.84 \quad (\pm 0.15mm) \tag{7}$$

$$D_D = 0.84H \quad (\pm 0.14mm) \tag{8}$$

Included in Table 2 are values for D_R and D_D determined from these correlations for comparison to the experimental values. As the correlations were developed from the experimental data to which the predicted values are compared, agreement is good.

The bubble departure frequency is plotted in Fig. 10 in terms of its non-dimensional frequency and non-dimensional gap height. Provided also is the data from the diabatic study, at a different (higher) pressure differential across the membrane. The non-dimensional frequency is written in terms of the Strouhal number

$$St = f_D \sqrt{\frac{H}{g}} \tag{9}$$

This form of the Strouhal number is based on the characteristic velocity used by Haberman [18] where

$$u \propto \sqrt{gD_D} \approx \sqrt{gH} \tag{10}$$

The characteristic dimension H used in the velocity term was chosen because of the proportional relationship between H and D_D presented in Eq. (7). The unconfined departure diameter D_{UD} was chosen as the scaling parameter for the non-dimensional gap height,

$$H^* = \left(\frac{H}{D_{UD}} \right)^{-1/2} \tag{11}$$

where the unconfined departure diameter D_{UD} was predicted from a static force balance at departure, which is presented later in this thesis.

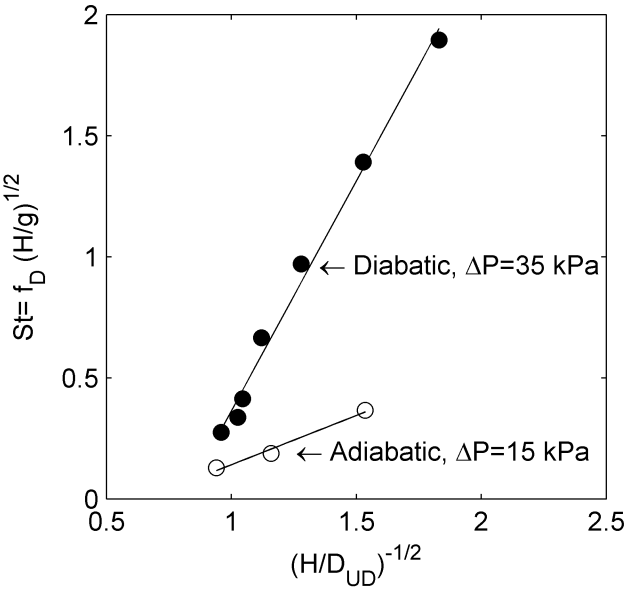

Figure 10: Non-dimensional departure frequency vs dimensionless gap height [1].

Linear regression was performed on the adiabatic data presented in Fig. 10 that resulted in a correlation relating the non-dimensional frequency to the non-dimensional gap height, where the standard error of the fit is reported in parenthesis

$$St = 0.41 \left(\frac{H}{D_{UD}} \right)^{-1/2} - 0.27 \quad (\pm 0.03) \tag{12}$$

As expected, based on previous observations made for Fig. 9, the departure frequency, f_D, is inversely proportional to gap height, H. As mentioned earlier with respect to the observation made for Fig. 9, more adiabatic data will need to be analyzed in order to confirm this trend. However, as was discussed in the study by Fox et al. [1] the trend is in agreement with what is observed in diabatic confined extraction. Also to be noted is the difference in slope between the diabatic and the adiabatic cases. This suggests that the bubble departure frequency may also be related to the pressure drop across the membrane.

4.3.4 Observations on the Time Between Events

The time interval between events are presented in Fig. 11 for each test case for both the diabatic and adiabatic studies. All adiabatic test cases show no appreciable wait time between successive bubbles, which is to be expected for constant flow conditions through the orifice. The time between inception and rupture for confined bubbles decreases with decreasing gap height. The time between contact and rupture appears to be independent of gap height, which suggests the time required for the thin film between the bubble and the extraction surface to drain is also independent of gap height. Although there is no clear trend present for the time between bubble rupture and departure, it is expected that with the inclusion of more data this time will decrease with smaller gap heights, as seen in the diabatic case studied by Fox et al. [1]. The time between bubble departure and extinction decreases with a decrease in gap height, which is thought to be a result of a smaller volume needing to be extracted after a bubble's departure from the orifice. Another notable feature of Fig. 11 is that for the adiabatic case of $H = 3.25\ mm$ the departure time is slightly longer than for the unconfined case. This may be due to the fact that for large gap heights, where $H \approx D_{UD}$, a bubbles diameter can actually grow larger than that for the unconfined case, with the additional growth taking place during the time it takes for the bubble to rupture after making contact with the extraction surface.

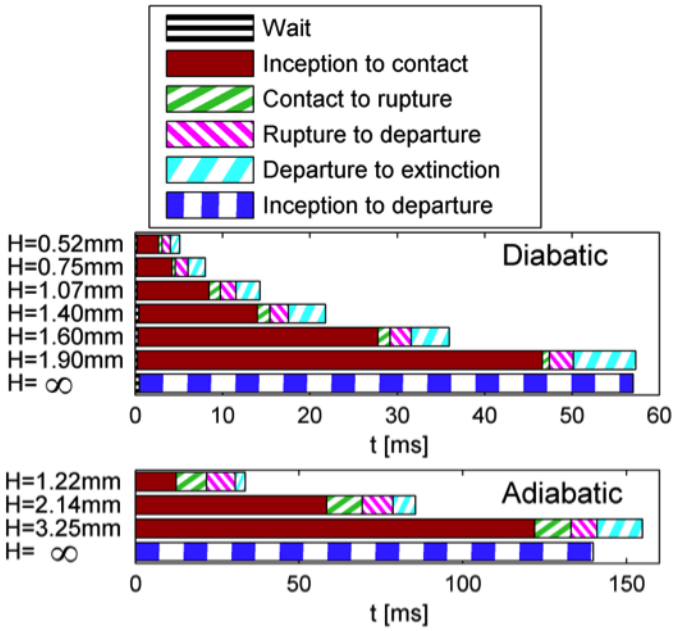

Figure 11: Time between events [1]

4.3.5 Regimes of the Extraction Process

Three distinct regimes were observed during confined extraction of Type 1 bubbles, which are illustrated in Fig. 12. They are defined as follows:

- Regime I - Linear volumetric bubble growth occurs between its inception (I) and rupture (R), as can be observed in Fig. 13. This is to be expected because the volumetric flow rate through the orifice is constant. The bubble in this regime is illustrated in Fig. 12a where the bubble is attached to the orifice but has not yet ruptured at the extraction surface.

- Regime II - This regime addresses bubble growth in the non-linear region between rupture (R) and departure (D) as can be observed in Fig. 13. It is thought that the non-linearity in this region is due to the dynamic nature of the three phase contact line at the extraction surface following rupture, which results in variable extraction rates. The bubble in this regime is illustrated in Fig. 12b where the bubble is still attached to the orifice while also being

extracted through the porous membrane at the extraction extraction surface.

- Regime III - Based on observations made in Fig. 13, bubble growth in the regime between departure (D) and extraction (E) has been approximated as linear. Because of the linearity in this region, it is expected that the extraction area has reached some maximum and stabilized by the time departure occurs. The bubble in Regime III, as illustrated in Fig. 12c is no longer attached to the orifice and is only being extracted through the extraction surface.

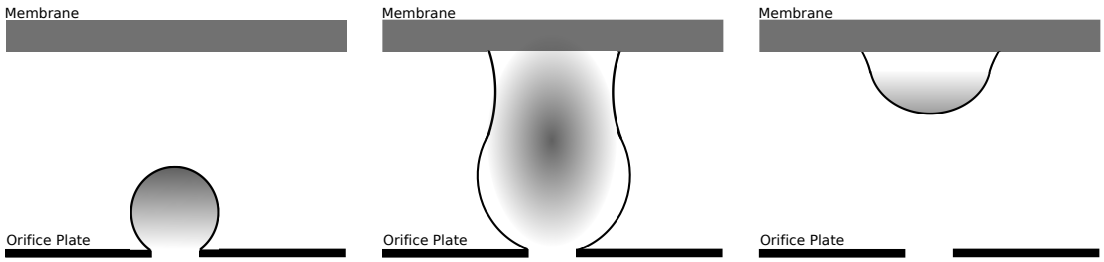

(a) Regime I (b) Regime II (c) Regime III

Figure 12: Illustrations of the three distinct regimes of bubble growth during extraction

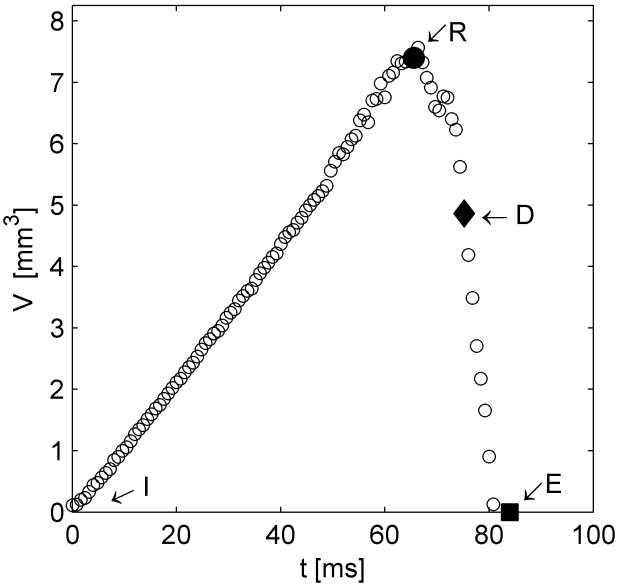

Figure 13: Volume of a bubble as a function of time at a gap height of $H = 2.14\ mm$ [1]

5 Model Development

The inherent limitations of correlations motivates the development of a theoretical model to predict a bubble's departure diameter and departure frequency. Bubble departure diameter and departure frequency for the unconfined case is well characterized by a model based on one proposed by Thorncroft [15] for horizontal pool boiling. That being said, a lack of understanding of three phase contact line dynamics post bubble rupture (R) at the extraction surface is preventing the full development of a model for confined conditions. Covered in this section are the beginning stages of a model's development, where in the mean time, empirical data will be used to show how the model should be employed pending further investigation of the three phase contact line after rupture. Points in this section are also made to facilitate a discussion of current knowledge gaps.

5.1 Unconfined Force Balance

Thorncroft et al. [15] performed a thorough assessment of forces acting on a bubble during its growth and developed a criterion for bubble departure under horizontal pool boiling conditions

$$F_B - F_{\sigma_{sup}} - F_G = 0 \tag{13}$$

where the forces included are the net buoyant force, surface tension force at the boiling surface, and growth force, all of which are illustrated in Fig. 14a, and are defined as

$$F_B = \frac{\pi D^3 g \left(\rho_l - \rho_g\right)}{6} \tag{14}$$

$$F_{\sigma_{sup}} = \pi \sigma d_w \sin \theta_{sup} \tag{15}$$

and

$$F_G = 2\pi \rho_l r^2 \dot{r}^2 \tag{16}$$

Assumed is spherical bubble growth, where r and $\dot{r}$ are the bubble radius and radial growth rate, respectively. For a pinned three-phase contact line at an orifice, as is the case in this study, $d_w = d_o$. Note that since the bubble is pinched off at the moment of departure the equivalent force due to momentum through the orifice may be neglected. A constant contact angle at the supply surface, θ_{sup}, was chosen to be 90°. This value was chosen because it yielded the best predicted unconfined departure diameter which is presented in Table 2.

5.2 Proposed Force Balance for a Confined Extraction

Figure 14b illustrates the forces for the confined case where departure occurs at the instant Regime II ends and Regime III begins. The additional forces that are included for the confined case, compared with the unconfined case, are the surface tension force at the extraction surface $F_{\sigma_{ext}}$ and the equivalent force due to the momentum of gas through the extraction surface $(\dot{m}v)_{ext}$. Including these additional forces, Thorncroft's [15] departure criteria becomes

$$F_B - F_G - F_{\sigma_{sup}} + F_{\sigma_{ext}} - (\dot{m}v)_{ext} = 0 \tag{17}$$

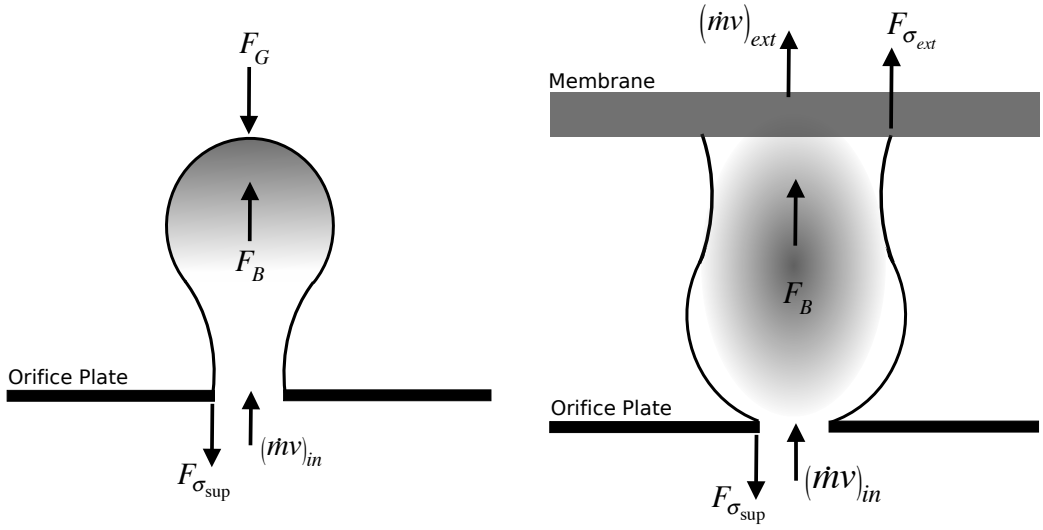

(a) Unconfined (b) Confined in Regime II

Figure 14: A comparison of forces at departure

An additional simplification can be made if Thorncroft's [15] development of the growth force, F_G, is considered. The growth force in Thorncroft's [15] study was developed by considering the pressure force imparted on a bubble during its vertical growth due to the displacement of the fluid above it. Thus, F_G is largest in the beginning stages of growth where $D_{bub} \sim t^{1/3}$. Based on this reasoning, the growth force is taken to be zero after the bubble makes contact with the extraction surface because it is no longer growing vertically. Applying this simplification to Eq. (17) the departure criterion becomes

$$F_B - F_{\sigma_{sup}} + F_{\sigma_{ext}} - (\dot{m}v)_{ext} = 0 \tag{18}$$

The equivalent force due to the momentum of gas through the extraction surface is an application of Darcy's law using the area of extraction, A_{ext}, as shown by Capello [19], where the area of extraction, A_{ext}, is taken as the area of the bubble in contact

with the extraction surface

$$(\dot{m}v)_{ext} = \frac{\rho V_e^2}{A_{ext}} = \rho d_{ext}^2 \frac{\pi}{4} \left(\frac{\kappa \Delta P}{\mu_g \delta} \right)^2 \tag{19}$$

The force due to surface tension at the extraction surface is defined as

$$F_{\sigma_{ext}} = \pi \sigma d_{ext} \sin \theta_{ext} \tag{20}$$

Substituting Eqns. (14), (15), (20), and (19) into Eq. (18) yields

$$\frac{\pi D^3 g \left(\rho_l - \rho_g\right)}{6} - \pi \sigma d_o \sin \theta_{sup} + \pi \sigma d_{ext} \sin \theta_{ext} + \rho d_{ext}^2 \frac{\pi}{4} \left(\frac{\kappa \Delta P}{\mu_g \delta} \right)^2 = 0 \tag{21}$$

where at departure, the diameter in the bouyancy term is the departure diameter, D_D,

$$\frac{\pi D_D^3 g \left(\rho_l - \rho_g\right)}{6} - \pi \sigma d_o \sin \theta_{sup} + \pi \sigma d_{ext} \sin \theta_{ext} + \rho d_{ext}^2 \frac{\pi}{4} \left(\frac{\kappa \Delta P}{\mu_g \delta} \right)^2 = 0 \tag{22}$$

Solving for the departure diameter using this equation requires knowlege of the contact angles at both the supply surface (orifice), θ_{sup}, and the extraction surface, θ_{ext}, as well as the diameter of the extraction area, d_{ext}. The value used for the contact angle at the supply surface was choosen to be 90° because that is what was used in the unconfined model which produced good results.

Until a more thorough study of the three phase contact line at the extraction surface is conducted, the values for the diameter of the three phase contact line, d_{ext}, and the contact angle at the three phase contact line, θ_{ext}, are assessed as follows:

- The diameter of extraction, d_{ext}, was determined experimentally by Fox et al. [1], by measuring the slope post bubble departure (D) in volume versus time plots, where the volumetric flow rate becomes relatively constant as seen in Fig. 13. The d_{ext} that yielded the volumetric flow rate was found to be approximately equal to D_D. Therefore the diameter of extraction, d_{ext}, used in Eq. (22), is set to the departure diameter, D_D, provided by Eqn. (8).

- Originally a value of 125° was used for the contact angle at the extraction surface, which was measured by using a sessile drop on the hydrophobic membrane [1]. This yielded poor results for D_D though, which is thought to be partially attributed to the pressure drop across the membrane creating an additional upwards force on the bubble and to the difference in the orientation with respect to gravity. Therefore, the contact angle at the extraction surface was adjusted to yield results for D_D that matched the experimental results in Table 2. The results for θ_{ext} are provided in Table 3.

Regardless of the shortfalls of the model at this time, the various force components at departure were calculated and listed in Table 3. Evident from Table 3 is that for confined Type 1 bubbles, the mechanism for departure is the additional surface tension force at the membrane. As the gap height, H, is reduced, the surface tension force at the extraction surface, $F_{\sigma_{ext}}$, increases as noted from Eq. (20). This is reflected by a decrease in the contact angle with an increase in d_{ext}. All thermophysical properties were assessed at $20°C$ and 1 atm, and the value used for the permeability constant κ was 7.5×10^{-15} m^2, which was experimentally determined by Cappello [19].

Table 3: Magnitude of forces at departure using a static force balance. Contact angles used at the extraction surface were solved for based on D_D and d_{ext} that are determined experimentally

H $[mm]$	D_D $[mm]$	F_G $[\mu N]$	$F_{\sigma_{sup}}$ $[\mu N]$	F_B $[\mu N]$	$(\dot{m}v)_{ext}$ $[\mu N]$	$F_{\sigma_{ext}}$ $[\mu N]$	θ_{ext} $[deg]$
1.22	0.97	N/A	116	4.67	0.155×10^{-6}	111	152
2.14	1.91	N/A	116	35.7	0.476×10^{-6}	80	169
3.49	2.68	N/A	116	98.6	1.27×10^{-6}	16.3	178
∞	2.85	0.13	116	116	N/A	N/A	N/A

In this study the contact angle at the supply surface was set at a constant 90° because that is what yielded the best results for unconfined bubble departure diameters, D_D. Figure 15 compares the contact angles at the supply surface for each test case in this study one frame before bubble departure. It appears as though the supply contact angle is not affected by variation of gap heights at departure, which suggests that the value used for unconfined departure may be justified for use under confined conditions. It may be beneficial to study this further by capturing video images at a higher frame rate.

(a) $H = 1.22mm$ (b) $H = 2.14mm$ (c) $H = 3.25mm$ (d) Unconfined

Figure 15: Observations of the contact angle at the supply surface the frame before bubble departure for the test cases included in this study.

5.3 Proposed Bubble Diameter Model

In order to predict bubble departure frequencies, a time-varying bubble diameter model is needed. The bubble diameter model is developed by assessing the volumetric growth rate of a bubble based on the conservation of mass while assuming no

variations in density. Volumetric flow rates through the orifice and/or the extraction surface are considered. Which flow rates to include in the analysis is determined by the regime (Fig. 12). The volumetric flow rate through the orifice is

$$\dot{V}_o = const \tag{23}$$

where the volumetric flow rate through the membrane is an application of Darcy's law using the area of extraction A_{ext}

$$\dot{V}_e = \frac{\kappa \Delta P A_{ext}}{\mu_g \delta} \tag{24}$$

5.3.1 Regime I

The bubble in Regime I experiences a constant growth rate as seen in Fig. 13 between inception (I) and the instant before Rupture (R). The diameter in Regime I, D_I, can be determined by integrating

$$\frac{dV_I}{dt} = \dot{V}_o \tag{25}$$

between the limits of $0 \leq t \leq t_R$ and $0 \leq V \leq V_R$ resulting in

$$D_I(t) = \sqrt[3]{\frac{6\dot{V}_o}{\pi} t} \tag{26}$$

Ideally, the time of bubble rupture, t_R, would be determined theoretically by interfacial surface science, which would be used with Eq. (26) to model a bubbles growth until rupture (R). Until then, the diameter of the ruptured bubble, D_R, is determined by the correlation in Eq. (7) and used as the condition for transitioning from Regime I to Regime II.

5.3.2 Regime II

After bubble rupture (R), the volumetric flow rate through both the orifice and the the extraction surface must be simultaneously considered until departure (D). The flow rate in this regime is grossly approximated as linear as can be observed in Fig. 13. In actuality the area of extraction at the extraction surface is dynamic. The dynamic nature of the area of extraction will need to be studied further in order to increase the accuracy of this model. The diameter in Regime II, D_{II}, can be determined by integrating

$$\frac{dV_{II}}{dt} = \dot{V}_o - \dot{V}_e \tag{27}$$

for $t_R \leq t \leq t_D$ and $V_R \leq V \leq V_D$ resulting in

$$D_{II}(t) = \sqrt[3]{\frac{6}{\pi}\left[V_R + \dot{V}_o(t - t_R) - \frac{\kappa \Delta P A_{ext,II}}{\mu_g \delta}(t - t_R)\right]} \tag{28}$$

Until the dynamic nature of the area of extraction can be studied further, a linear approximation of its growth is made

$$A_{ext,II} = A_{ext,III}\frac{t - t_R}{t_{d,St} - t_R} \tag{29}$$

where, $t_{d,St}$, used for scaling and is determined by the Strouhal correlation in Eq. (12). Additionally, the area of extraction at departure is estimated by experimental observation, where as stated earlier $D_{ext} \approx D_D = 0.84H$. Therefore, the area of extraction for Regime III will be estimated as

$$A_{ext,III} = \frac{\pi}{4}(0.84H)^2 \tag{30}$$

The departure diameter D_D, predicted from Eq. (8) is used as the condition for transitioning from Regime II to Regime III.

5.3.3 Regime III

After departure (D) from the orifice, only the volumetric flow rate through the extraction surface needs to be considered. The area of extraction after departure considered constant based on the observations made between departure (D) and extraction (E) in Fig. 13. The diameter in Regime III, D_{III} can be determined by

$$\frac{dV_{III}}{dt} = -\dot{V}_e \tag{31}$$

for $0 \leq t \leq t_D$ and $0 \leq V \leq V_D$ resulting in

$$D_{III}(t) = \sqrt[3]{\frac{6}{\pi}\left[\dot{V}_D - \frac{\kappa \Delta P A_{ext,III}}{\mu_g \delta}(t - t_D)\right]} \tag{32}$$

An example of model results are presented in Fig. 16, where it is plotted along with the experimental data presented in Fig. 8. Rupture (R) and departure (D) diameters are fairly well predicted, although this would be expected since the values that are used for transition between regimes in the model are determined from the correlations developed from experimental data to which the model is being compared. Time of rupture is fairly well predicted based on the reasoning just discussed. It is thought that interfacial surface science will need to be applied in order to determine t_R theoretically. Also, a theoretical model based on interfacial surface science may also be developed for the dynamic area of extraction, A_{ext}, after rupture, which would allow for the theoretical determination of t_D. The usefulness of this model will be its ability to predict bubble departure frequency. The bubble departure frequency, f_D, can be predicted by taking the inverse of the total time between inception (I) and departure (D) assuming no wait time. Predictions based on this model are included in Table 2.

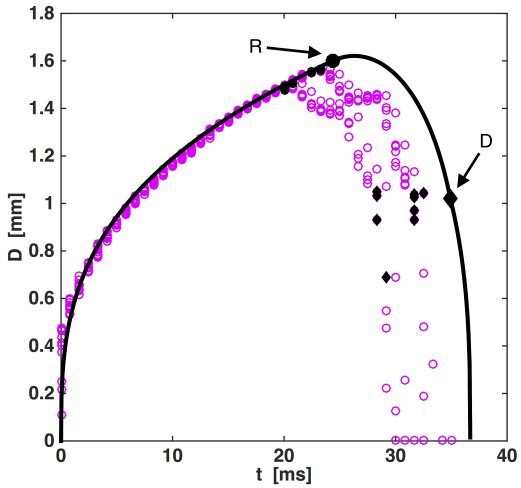

Figure 16: Bubble diameter model results overlaid on Fig. (8) data for a gap height of $H = 1.22\ mm$.

6 Conclusions and Recommendations

An adiabatic experiment was designed to study the hydrodynamics of the extraction process. The experimental test facility was successful in that it produced bubbles that grew at a constant growth rate with no wait times between successive bubbles. Additionally, experimental results closely trended those from the diabatic study that was done in parallel by Fox et al. [1]. More data will need to be taken and analyzed to confirm this. Additionally an image processing algorithm was developed that was successful in isolating the bubble from its environment that yielded consistency in the data reduction process.

High speed video was taken of bubbles that were formed at a submerged orifice and extracted through a confining hydrophobic membrane. The gap height, or height of the extraction surface above the supply surface was varied and its effect on bubble dynamics was studied. This study focused on bubbles that ruptured before they departed from the supply surface. The growth and extraction cycle of these bub-

bles were broken down into three different regimes: Regime I - the inception and subsequent growth of the bubble until the instant it ruptures on the extraction surface; Regime II - from the moment of rupture until the instant of departure; Regime III - from the moment of departure to the extinction of the bubble. Marking the transition between these regimes are the time and diameter at which the bubble ruptures and the time and diameter at which the bubble departs from the supply surface.

Correlations were developed that can be used to determine the bubble's rupture diameter and the bubble's departure diameter as a function of gap height. A non dimensional relationship has also been developed that can be used to predict the departure frequency of the bubble. It was found that the departure diameter of a bubble is proportional to the gap height and that the bubble departure frequency is inversely proportional to the gap height. Hence, the bubble departure frequency and diameter can be controlled by varying the gap height between the extraction surface and the supply surface. However, these correlations are strictly limited to the conditions for which the data were taken. A more general method for predicting D_D and f_D under a wide range of conditions was undertaken that includes a static force balance to predict D_D and a bubble diameter model based on conservation of mass and Darcy's law that allows for the prediction of f_D with knowledge of D_R and D_D.

The foundation of a force balance has been presented that can be used to predict the departure diameter of bubbles under confined conditions. After the bubble ruptures, the area of extraction is dynamic. The dynamic nature of the extraction area determined by the three-phase contact line is one of the knowledge gaps that needs to be filled before this model can be developed further. Also to be investigated is the contact angle at the extraction surface. The contact angle at the supply surface appears to be unaffected by varying gap height, but it is recommended that this is

studied further with video taken at higher frame rates before this conclusion can be made.

A study of the magnitude of forces present at bubble departure under confined conditions at varying gap heights showed that the surface tension force at the extraction surface is the mechanism for bubble departure. This may be of use in aerospace applications where micro-gravity conditions prevents bubble departure.

The foundations of a transient bubble model were also presented that currently uses values determined by the correlations developed to predict bubble departure frequencies. Once a theoretical model is developed that can predict bubble rupture and three phase contact line dynamics, perhaps by applying inter-facial surface science, this model will be of more value.

References

[1] R. G. Fox, C. D. Juarez, D. V. Pence, and J. A. Liburdy, "Altering bubble dynamics via in-situ vapor extraction," *Heat Transfer Engineering*, submitted 2015.

[2] H. F. Hamann, J. Lacey, A. Weger, and J. Wakil, "Spatially-resolved imaging of microprocessor power (simp): hotspots in microprocessors," in *Thermal and Thermomechanical Phenomena in Electronics Systems, 2006. ITHERM'06. The Tenth Intersociety Conference on*, pp. 5–pp, IEEE, 2006.

[3] J. Kong, S. W. Chung, and K. Skadron, "Recent thermal management techniques for microprocessors," *ACM Computing Surveys (CSUR)*, vol. 44, no. 3, p. 13, 2012.

[4] A. N. Nowroz, R. Cochran, and S. Reda, "Thermal monitoring of real processors: techniques for sensor allocation and full characterization," in *Proceedings of the 47th Design Automation Conference*, pp. 56–61, ACM, 2010.

[5] M. A. Apreotesi, *Microscale thermal management utilizing vapor extraction from a fractal-like branching heat sink*. PhD thesis, 2007.

[6] W. Qu and I. Mudawar, "Measurement and prediction of pressure drop in two-phase micro-channel heat sinks," *International Journal of Heat and Mass Transfer*, vol. 46, no. 15, pp. 2737–2753, 2003.

[7] M. P. David, T. Khurana, C. Hidrovo, B. L. Pruitt, and K. E. Goodson, "Vapor-venting, micromachined heat exchanger for electronics cooling," in *ASME 2007 International Mechanical Engineering Congress and Exposition*, pp. 951–960, American Society of Mechanical Engineers, 2007.

[8] M. P. David, J. Miler, J. E. Steinbrenner, Y. Yang, M. Touzelbaev, and K. E. Goodson, "Hydraulic and thermal characteristics of a vapor venting two-phase microchannel heat exchanger," *International Journal of Heat and Mass Transfer*, vol. 54, no. 25, pp. 5504–5516, 2011.

[9] K. Goodson, A. Rogacs, M. David, and C. Fang, "Volume of fluid simulation of boiling two-phase flow in a vapor-venting microchannel," *Frontiers in Heat and Mass Transfer (FHMT)*, vol. 1, no. 1, 2010.

[10] A. Fazeli, M. Mortazavi, and S. Moghaddam, "Hierarchical biphilic micro/nanostructures for a new generation phase-change heat sink," *Applied Thermal Engineering*, 2015.

[11] D. Gerlach, G. Biswas, F. Durst, and V. Kolobaric, "Quasi-static bubble formation on submerged orifices," *International Journal of Heat and Mass Transfer*, vol. 48, no. 2, pp. 425–438, 2005.

[12] D. Dyson, "Contact line stability at edges: comments on gibbs's inequalities," *Physics of Fluids (1958-1988)*, vol. 31, no. 2, pp. 229–232, 1988.

[13] K. Terasaka and H. Tsuge, "Bubble formation under constant-flow conditions," *Chemical Engineering Science*, vol. 48, no. 19, pp. 3417–3422, 1993.

[14] A. Satyanarayan, R. Kumar, and N. Kuloor, "Studies in bubble formation—ii bubble formation under constant pressure conditions," *Chemical Engineering Science*, vol. 24, no. 4, pp. 749–761, 1969.

[15] G. Thorncroft and J. F. Klausner, "Bubble forces and detachment models," *Multiphase Science and Technology*, vol. 13, no. 3&4, 2001.

[16] J. D. Bernardin, I. Mudawar, C. B. Walsh, and E. I. Franses, "Contact angle temperature dependence for water droplets on practical aluminum surfaces," *International Journal of Heat and Mass Transfer*, vol. 40, no. 5, pp. 1017–1033, 1997.

[17] J. Xie, X. Zhu, Q. Liao, H. Wang, and Y.-D. Ding, "Dynamics of bubble formation and detachment from an immersed micro-orifice on a plate," *International Journal of Heat and Mass Transfer*, vol. 55, no. 11, pp. 3205–3213, 2012.

[18] W. Haberman and R. Morton, "An experimental investigation of the drag and shape of air bubbles rising in various liquids," tech. rep., DTIC Document, 1953.

[19] N. Cappello, D. Pence, and J. Liburdy, "Mass transport limitations through porous hydrophobic membranes," in *ASME 2013 Fluids Engineering Division Summer Meeting*, pp. V01CT17A017–V01CT17A017, American Society of Mechanical Engineers, 2013.

A Photographs of Experimental Set-up

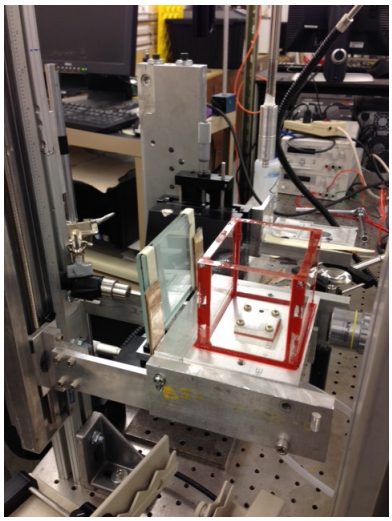

Figure 17: Photo of test chamber, halogen light, and light diffuser

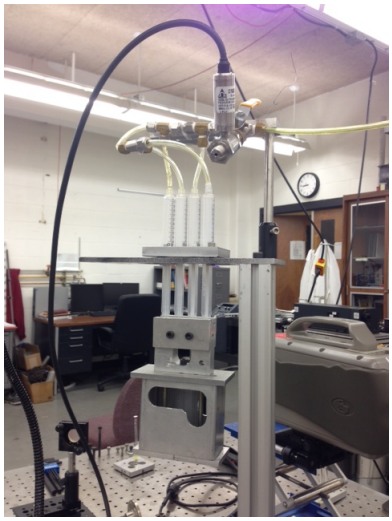

Figure 18: Photo of weights hanging from 10 *ml* syringes to create a vacuum in the extraction chamber.

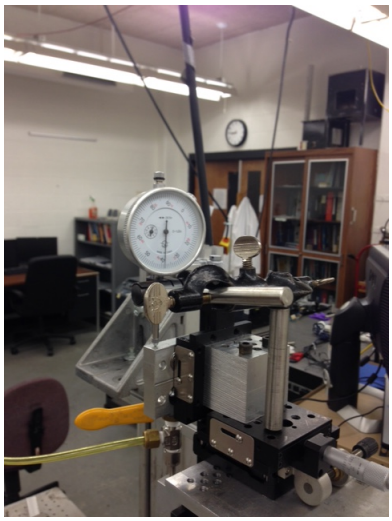

Figure 19: Photo of dial indicator that was used to measure relative gap height while collecting data

B Design Drawings

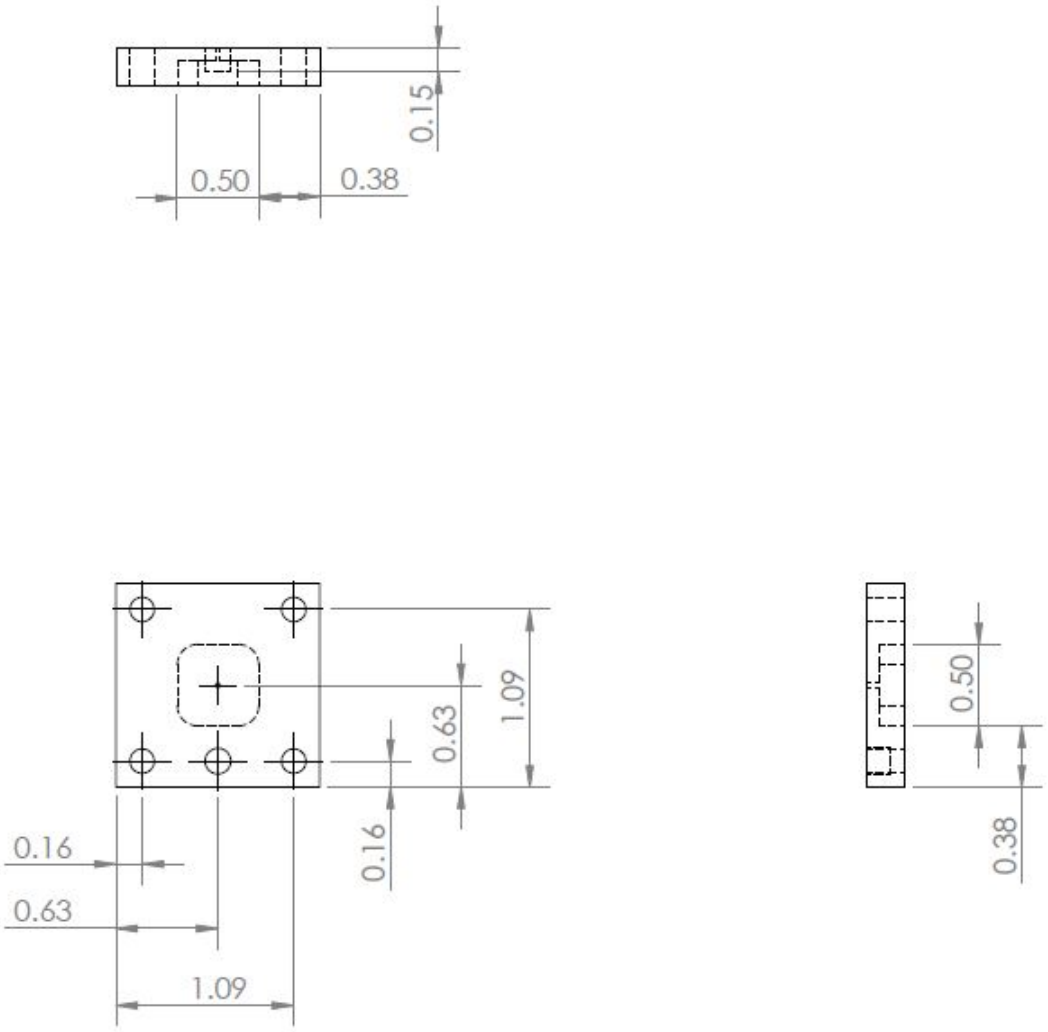

Figure 20: Orifice plate drawing. All units are in inches

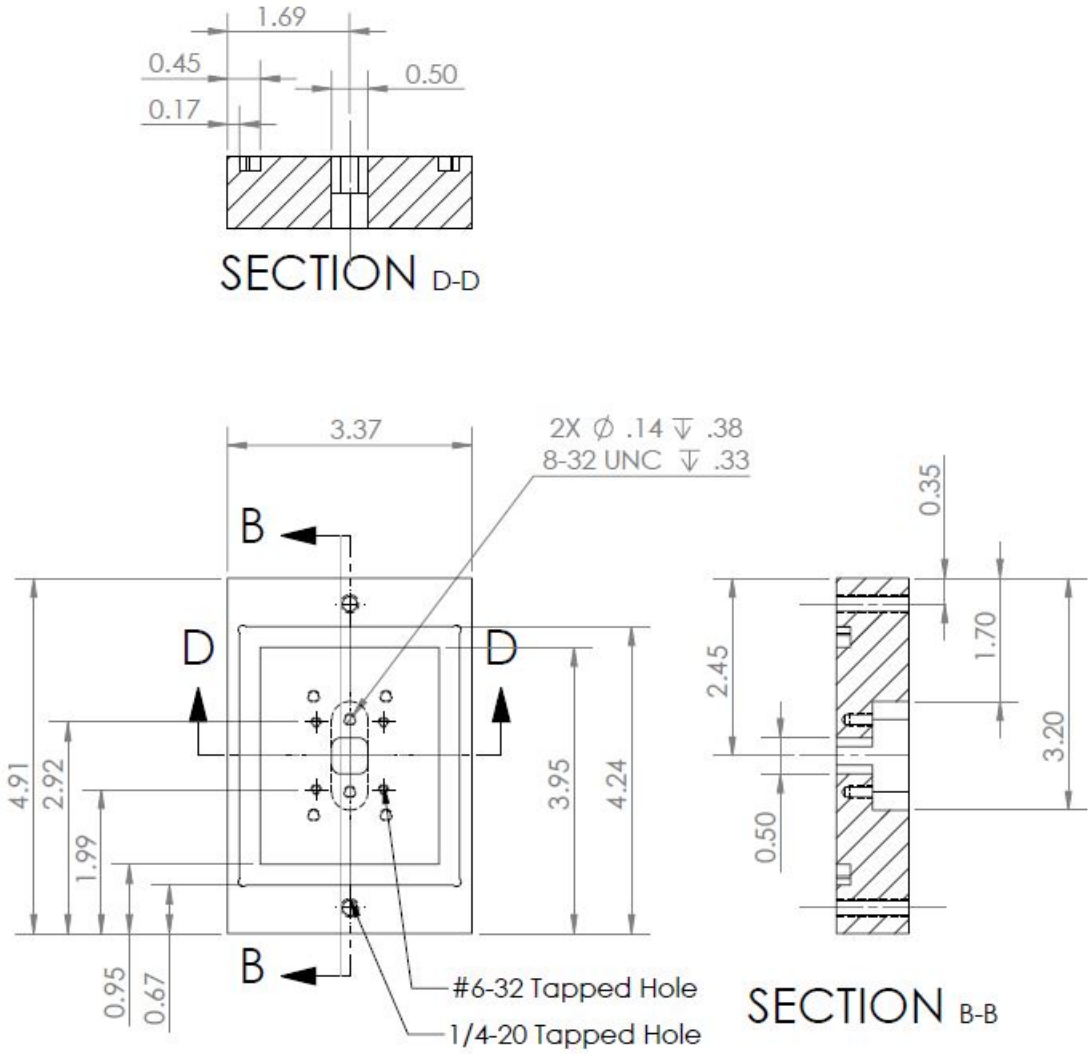

Figure 21: Base of test chamber drawing. All units are in inches

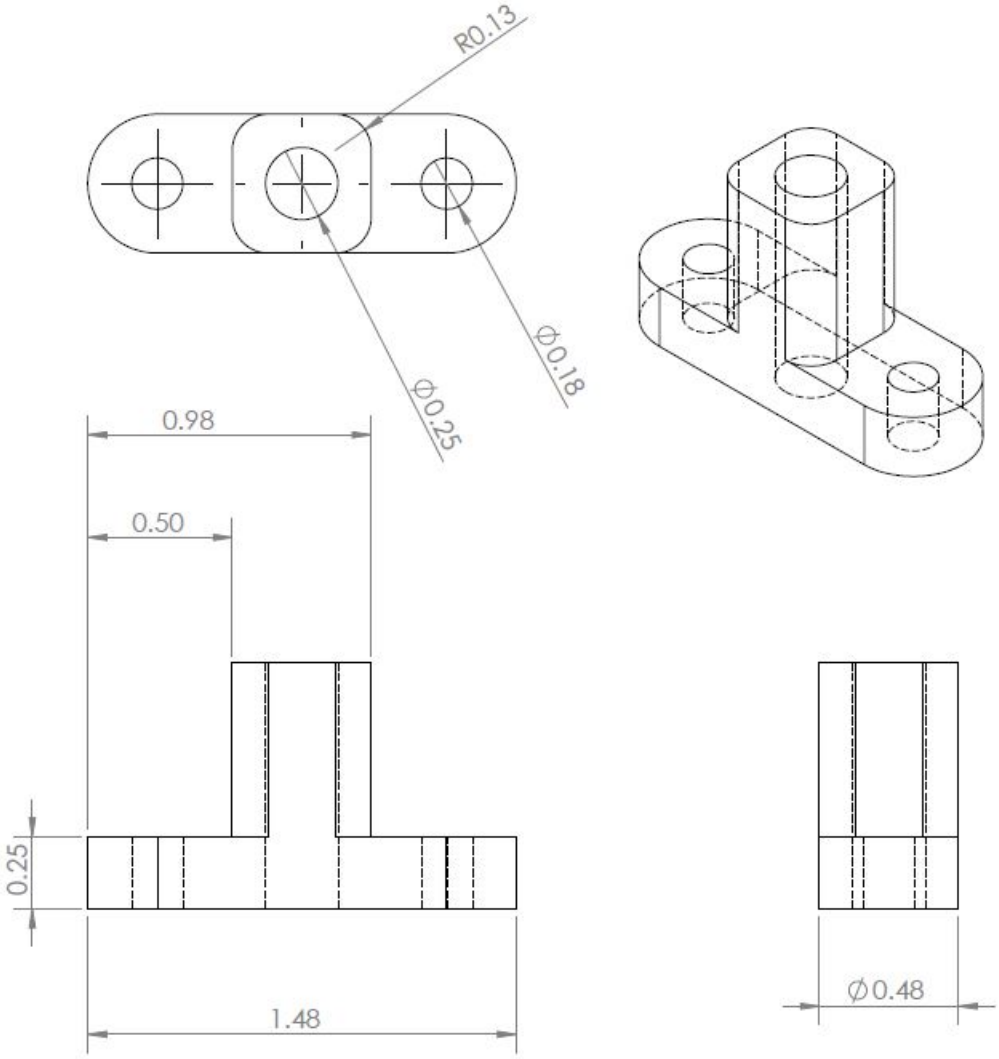

Figure 22: Membrane compactor drawing. All units are in inches

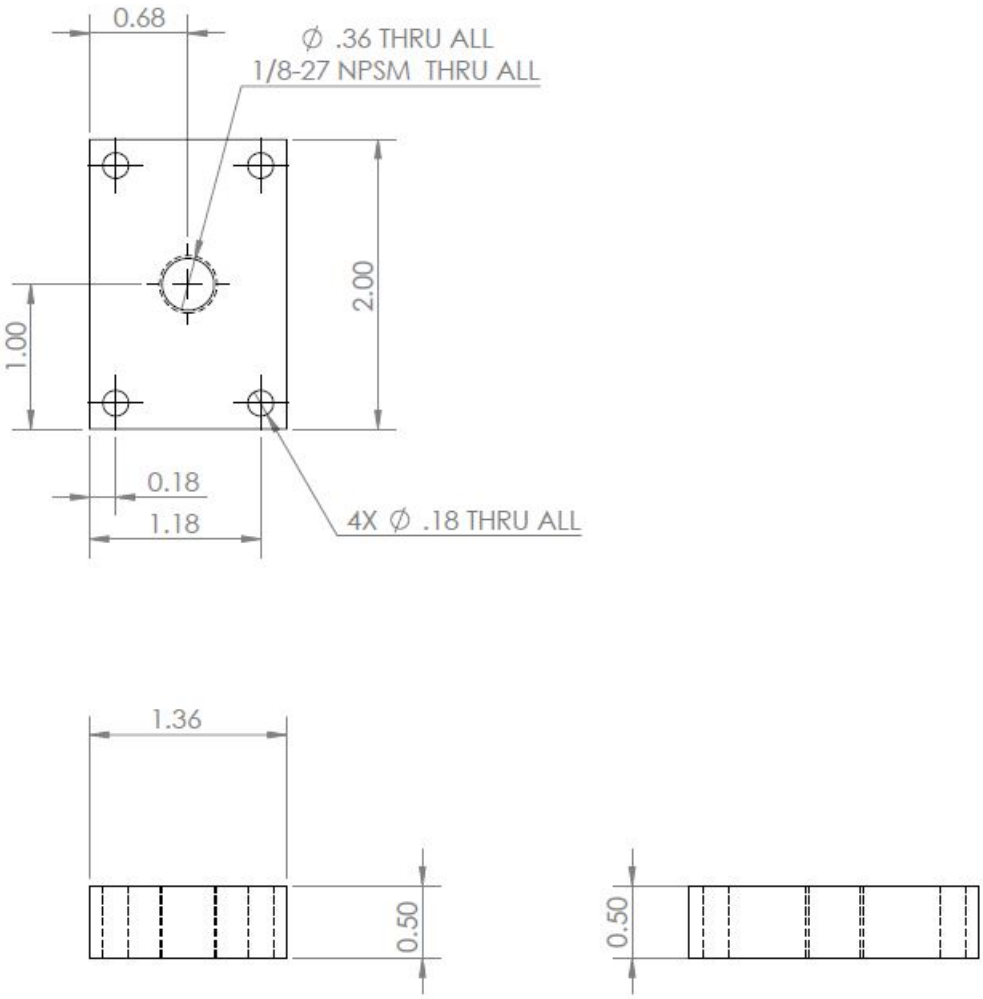

Figure 23: Inlet plate drawing. All units are in inches

C MATLAB code

```
%Corey Juarez

clear
clc
close all

%Ask user for file names and user input
fprintf('Select the image file you would like to use for
calibration of pixel width\n')
[calimagefilename,PathName] = uigetfile('*.tif','Select the
calibration image file');
fprintf('Select the image file you would like to analize\n')
[imagefilename,PathName] = uigetfile('*.tiff','Select the image
file');
fprintf('Select the Excel file you would like to use for
input\n')
[excelfilename,PathName] = uigetfile('*.xlsx','Select the excel
file');

%%% collect user input
range1='D4:D11';
[parameters,txt,raw] = xlsread(excelfilename,1,range1); % Reading
user input from the excel spreadsheet
if parameters(3) ~= 0 % Only ask for the background file if the
option is selected
    fprintf('Select a background imgage file\n')
    [backgroundfile,PathName] = uigetfile('*.tiff','Select the
background image file');
end
%%% organizing user input from excel
cal_dimension = parameters(1); % bearing diameter in mm
calframe = parameters(2);
background_frame = parameters(3);
bottom_distance = parameters(4); % For cropping bottom of image
top_distance = parameters(5); % For cropping top of image
canny_threshold_H = parameters(6); % upper threshold value to be
< 1
canny_threshold_L = parameters(7);  % Lower threshold value to be
< 1
T = [canny_threshold_L,canny_threshold_H]; % canny Treshold
vector
Frame_Matrix = txt{1}; %range for reading frame matrix in excel
Frame = xlsread(excelfilename,1,Frame_Matrix); % Reading and
storing the frame matrix from the excel spreadsheet

%Initializig zero matrices to ensure matrices of the same size
data=zeros(7,200);
total_bubble_volume=zeros(200,8);
effective_volume=zeros(200,8);
true_bubble_height = zeros(200,8);
max_bubble_width = zeros(200,8);
d_eff=zeros(200,8);
slice_width=zeros(1,200); %must be cleared after each use

%% Calibration
[X,map] = imread(calimagefilename,calframe);                %
Loading calibration image
         top = top_distance;                                %
```

```
number of pixels to interface of interest
         bottom = bottom_distance;                                  %
number of pixles to nucleation point
         leftmargin = 1;                                            %
unused automatic width cropping is not needed
         X = X(top:size(X,1)-bottom, leftmargin:size(X,2));  %
Cropping image
         [canny threshc] = edge(X,'canny',T);                       %
Edge detection using the canny method

% Displaying original and processed images
figure(1)
subplot(1,2,1); imshow(X); title('original')
subplot(1,2,2); imshow(canny); title('canny')

%selecting area of interest
figure(2)
area_of_interest=imcrop(canny);          % select area of
interest using rectangular selection tool, left click and select
crop
imshow(area_of_interest)                 % Display selected area

%determining pixel size
numrows=size(area_of_interest);

for i=1:numrows(1)
% For each (bearing) slice in the matrix perform the following
anlysis
    nonzero_locations=find(area_of_interest(i,:));
% find nonzero locations in horizontal slice of image
    empty=isempty(nonzero_locations);
% Checking to see if the previous vector is empty,
    if empty == 1
% If empty an error will occur so this if statement will keep
this from happening
        continue
% If empty, continue to next iteration
    end
    slice_width_in_pixels=max(nonzero_locations)-
min(nonzero_locations);
    slice_width(i)=slice_width_in_pixels;
% number of pixels in bearing slice
end
max_slice_width_in_pixels=max(slice_width);
pixel_width=cal_dimension/max_slice_width_in_pixels;
% mm pixel width and height 1:1
slice_width=zeros(1,200); %clearing matrix



 %% Processing bubble images
 numcol=size(Frame);                     % Determining the number
of bubbles
for j=1:numcol(2)                        % Do for Eeach bubble
    Bubble_Frames = Frame(:,j);          % Collecting the frame
numbers for a bubble
    N = length(Bubble_Frames);           % Number of frames
entered for each bubble
```

```
    if N == 0                               % If there are no frames
skip and contiue to next bubble
        continue
    end
    for k=1:N                               % This loop will execute
for every frame captured for the bubble
        if isnan(Frame(k,j)) == 1           % Check for NAN if NAN
in cell continue to next bubble
            continue
        end
        if Frame(k,j) == 0                  % A zero at begining of
column will cause the loop to skip to the next bubble
            continue
        end

        if background_frame ~= 0
            [Y,map] = imread(backgroundfile,background_frame);
            [Z,map] = imread(imagefilename,Frame(k,j)); %
Choosing the Nth frame of bubble j
            X = abs(Y-Z);                                   %
Subtracting background before edge detection
        elseif background_frame == 0                        % if
background subtraction is not being used
            [X,map] = imread(imagefilename,Frame(k,j)); %
Choosing the Nth frame of bubble j
        end

        top = top_distance;                                     %
Number of pixels to interface of interest
        bottom = bottom_distance;                               %
Number of pixles to atachment point on heated surface
        leftmargin = 1;                                         %
Unused automatic width cropping is not needed
        X=X(top:size(X,1)-bottom, leftmargin:size(X,2));    %
Cropped image
        [canny, threshc] = edge(X,'canny',T);                   %
Edge detection using the canny method Using the same filter as
above


        % Displaying original and processed images
        figure(1)
        subplot(1,2,1); imshow(X); title('original')
        subplot(1,2,2); imshow(canny); title('canny')

        %selecting area of interest
        figure(2)
        area_of_interest = imcrop(canny); % select area of
interest using rectangular selection tool, left click and selec
crop
        imshow(area_of_interest)          % Display selected area

        %determining volume and efffective diameter of the bubble
        numrows=size(area_of_interest);
        n=numrows(1);         %Establishing the number of rows in
the matrix as a counter
        bubble_volume = 0;    %initializing variable
        num_of_emptyrows = 0; %initialize counting variable
```

```
        bh = 0;
        for i=1:n             %For each row in the matrix perform
the following anlysis
            nonzero_locations=find(area_of_interest(i,:));    %
find nonzero locations in slice of image
            empty = isempty(nonzero_locations);               %
Checking to see if the previous vector is empty,
            if empty == 1                                     % If
empty an error will occur so this if statement will keep this
from happening
                continue                                      % If
empty, continue to next iteration
            end
            slice_width_in_pixels = max(nonzero_locations) -
min(nonzero_locations);
            if slice_width_in_pixels > 0
                bh = bh +1;
            end
            slice_width(i) = slice_width_in_pixels * pixel_width;
% mm Width of bubble slice
            slice_area = pi/4 * slice_width(i)^2;
% mm^2 Area of a bubble slice
            slice_height = pixel_width;
% mm Height of a slice is equal to the width of a pixel
            slice_volume = slice_area * slice_height;
% mm^3 Volume of a bubble slice
            bubble_volume = bubble_volume + slice_volume;
% Running total of bubble volume
        end
        % each bubble is assigned to a column j and each
parameter value is
        % assigned to a row k
        total_bubble_volume(k,j)=bubble_volume;       % mm^3
bubble volume for frame and bubble respectivley
        d_eff(k,j)=2*(3*bubble_volume/(4*pi))^(1/3);  % mm
effective bubble diameter
        true_bubble_height(k,j) = (bh)*slice_height;  % Height
for AR tracking
        max_bubble_width(k,j) = max(slice_width);     % Width for
tracking AR
        slice_width=zeros(1,200);                     % clearing
slice width matrix
    end
end
close all

%Write to excel
xlswrite(excelfilename,total_bubble_volume,2,'A3')
xlswrite(excelfilename,d_eff,2,'I3')
xlswrite(excelfilename,true_bubble_height,2,'Q3')
xlswrite(excelfilename,max_bubble_width,2,'Y3')
```